Journal Pre-proofs

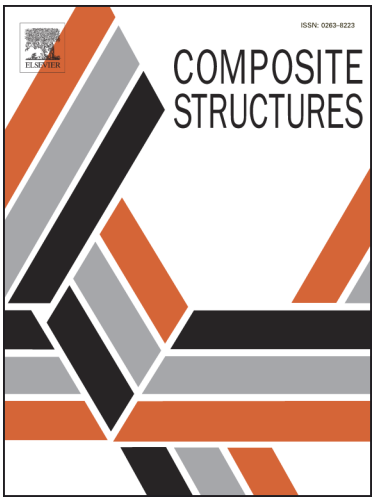

Experimental study of lag-twist coupling concept for rotor blade application

Huaiyuan Gu, Mohammadreza Amoozgar, Alexander D. Shaw, Jiaying Zhang, Chen Wang, Michael I. Friswell

PII: S0263-8223(21)00879-5
DOI: https://doi.org/10.1016/j.compstruct.2021.114417
Reference: COST 114417

To appear in: *Composite Structures*

Received Date: 9 September 2020
Accepted Date: 23 July 2021

Please cite this article as: Gu, H., Amoozgar, M., Shaw, A.D., Zhang, J., Wang, C., Friswell, M.I., Experimental study of lag-twist coupling concept for rotor blade application, *Composite Structures* (2021), doi: https://doi.org/10.1016/j.compstruct.2021.114417

Experimental study of lag-twist coupling concept for rotor blade application

Huaiyuan Gu[a,*], Mohammadreza Amoozgar[b], Alexander D. Shaw[a], Jiaying Zhang[a], Chen Wang[c], Michael I. Friswell[a]

[a] *College of Engineering, Swansea University, Swansea SA2 8PP, United Kingdom*
[b] *School of Computing and Engineering, University of Huddersfield, HD1 3DH, United Kingdom*
[c] *College of Aerospace Engineering, Nanjing University of Aeronautics and Astronautics, China*

Abstract

A novel passive twist morphing concept is examined for helicopter blades. The concept is demonstrated using a thin-walled rectangular composite beam created with symmetric layup to obtain bend-twist property. The twist of a rotor blade is proposed to be actuated though a movable mass at the blade tip which is able to provide a range of lagwise bending moment during rotation as a result of the centrifugal force. First a set of static bending test is performed which provides detailed characterisation of the deformation and strain distribution of the composite beam subjected to a number of bending loads. The results of the experiment fully verify numerical predictions including finite element approach (FE) and beam cross sectional analysis. A series of simulations are then conducted using the verified numerical model to demonstrate how the desired twist can be effectively achieved by manipulating the size and location of the mass.

Keywords: Morphing, rotor blade, composite material, bend-twist coupling, FE analysis

*Corresponding author
Email address: huaiyuan.gu@swansea.ac.uk (Huaiyuan Gu)

1. Introduction

The development of morphing technologies provide a wide range of strategies to allow for the adjustment of the blade configuration under different flight conditions to reach optimum aerodynamic performances[1, 2, 3]. Morphing achieved passively is particularly of interest due to the tremendous advantages of the energy saving and design simplicity [4]. A novel passive morphing concept, inertial twist, has been proposed in a recent study to be deployed in helicopter blades[5]. The concept involves introducing a bend-twist coupled composite beam and a movable mass to a rotor blade. Therefore the twist can be actuated during rotation as a result of the bending moment caused by the centrifugal force as illustrated in Figure 1. Although the basis of the concept and the aeroelastic stability of the mechanism has been explored through a simplified one-dimensional beam model[6], there is little experimental data to verify the results and examine the morphing strategy. The work described here aims to provide accurate experimental characterisation of the bend-twist behaviour achieved in the composite beam and a comprehensive demonstration of the morphing concept with the verified numerical models.

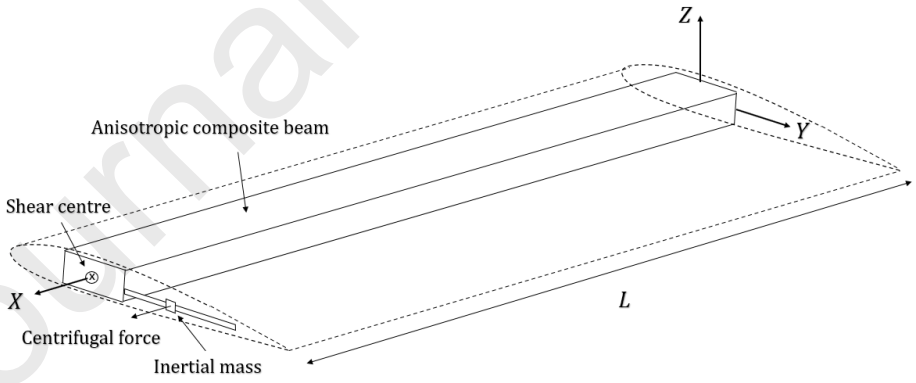

Figure 1: Schematic drawing of the inertial twist morphing concept.

A large body of research work has developed efficient morphing solutions with small penalties in cost and weight. To achieve this goal, a number of active

materials have been employed as actuators, which allow for the controlled shape of the blade without introducing the complexity of mechanisms [7, 8, 9]. The potential of piezoelectric materials in morphing applications has been widely explored. These materials can be deformed by electric current which is capable of introducing a local strain field on the surface. Lim et.al [10] deformed the trailing edge of a wing blade by embedding a stack of piezoelectric actuators into composite laminates, where a deflection angle of 5° was measured at 300V voltage input. In the work of Chen and Chopra [11], an array of orientated piezoelectric patches were embedded in the top and bottom surfaces of a rotor blade to obtain a controlled twist during rotation. However, the magnitude of the twist was limited by the torque generated by the piezoelectric patches, particularly with the presence of aerodynamic forces. It has been reported that approximately 0.1 degree twist was measured at an operating speed of 900 rpm. Shape memory alloys(SMA) are popular active materials, which are able to return to their original shape from any deformed state when the threshold temperature is reached. A pre-twisted SMA tube was employed by Ameduri and Concilio [12] to produce a spanwise twist in a rotor blade, where the torque was transmitted though the entire blade during the strain recovery process. Despite of the fact that a reasonable amount of twist can be achieved using the SMA actuator, the success of the method for rotor blades depends critically on the speed that the heat can be transmitted and absorbed away from the material. One possible solution for this is to use thermoelectric modules(TEMs) which are able to pump heat from one side to another with the aid of electric current [13]. The other issues of SMA actuators in morphing applications, such as heat treatment and bandwidth, have also been discussed in the work of Prahlad and Chopra[14].

Elastic coupling has been used extensively in morphing blades [15, 16, 17, 18]. The twist of the blade is often coupled by the axial and bending loads, which enables the direct control of the angle of attack. The coupling behaviour is most commonly obtained by the stiffness tailoring of composite laminates. Two types of configurations have been widely used which are referred to as the

symmetric and antisymmetric layups [19]. The symmetric layup provided the bend-twist coupling while the extension-twist coupling can be obtained from the antisymmetric layup. The Grumman X-29, a well-known forward-swept aircraft, utilised bend-twist coupled laminates to avoid aeroelastic divergence by making use of the coupled torque [20]. A number of metamaterials have been proposed as alternative candidates to produce the coupling effect. For example, the tension-twist coupling can be obtained from three-dimensional metamaterials which are able to convert the axial deformation to the cell rotation by using a series of inclined rods or faces[21, 22, 23]. A bend-twist coupled metamaterial has also been created by adding antisymmetrical features to the unit cell where an efficient coupling behaviour can be obtained[24].

In this paper, the inertial twist morphing concept is examined and demonstrated using a thin-walled composite beam manufactured with a symmetric layup configuration. First a number of static bending tests are performed and the measured results are compared with the numerical predictions. Then the verified numerical model was adopted to investigate the twist distribution of the beam subjected to a tip inertial mass under rotation. The results show the relationship among the twist angle, size and locations of the mass. Finally, a numerical analysis is performed to explore the optimum ply angle which is able to provide the highest actuation efficiency.

2. Experiment

2.1. Specimen fabrication

A rectangular thin-walled composite beam was built using the autoclave facility at the University of Bristol, with the outer dimensions as shown in Figure 2(a), where the thickness of the beam, T, was chosen based on the cross sectional size of the main rotor blade of the BO-105 helicopter [25]. The beam was fabricated by wrapping six layers of graphite/epoxy prepregs (Hexcel 8522) with fibre volume fraction of 0.55 over a rectangular mold with corner radius of 2.5mm cut from a Rohacell foam sheet(110 XT-HT). The foam was able to

resist a 7 bar pressure at 190°, which was capable of withstanding the required curing conditions [26]. A symmetric layup configuration was used to obtain the bend-twist property as illustrated in Table 1 and Figure 2(a). The prepreg widths were cut to size and laid up in a way that the joints were staggered around the corner to avoid resin or fiber-rich areas, as shown in Figure 2(b), where the prolonged length, w_p, was approximately 1 mm at each corner.

A vacuum pump was used after laying every two laminates to remove possible air bubbles between the layers. After finishing the layup process, a release film was wrapped around the beam to maintain a good surface condition. Next the entire beam was covered by a breather layer and placed into a vacuum bag for the curing process, as shown in Figure 3. The autoclave was set to provide a curing pressure of 5 bar and a temperature of 185°, following the recommendation of the prepreg supplier. Finally the vacuum bag, breather layer and release film were removed from the beam at the end of the curing cycle.

Top wall	Bottom wall	Left wall	Right wall
$[45]_6$	$[45]_6$	$[+45/-45]_3$	$[+45/-45]_3$

Table 1: Layup of the thin-walled rectangular beam.

2.2. Bending test

A set of cantilever beam tests was conducted to characterise the bend-twist property and strain distribution of the composite beam subjected to a number of bending loads. At the supporting end, the beam was firstly slotted into a steel hub built with a 80 mm long sleeve and bonded using epoxy resins. The hub was then bolted to a rigid fixture made from 8 mm thick steel plates shown in Figure 4 and 5(a). The bending loads were applied by hanging incremental weights on the beam. A small fixture was installed at the tip consisting of two semi-rectangular metal pieces with a 500mm screw bar fixed in place using two locking nuts, allowing for the weights to be applied at different locations along the Z-axis as shown in Figure 5(b), to enable the torque loading, T_x, to be varied independently of the bending moment, M_z. Five equally spaced loading

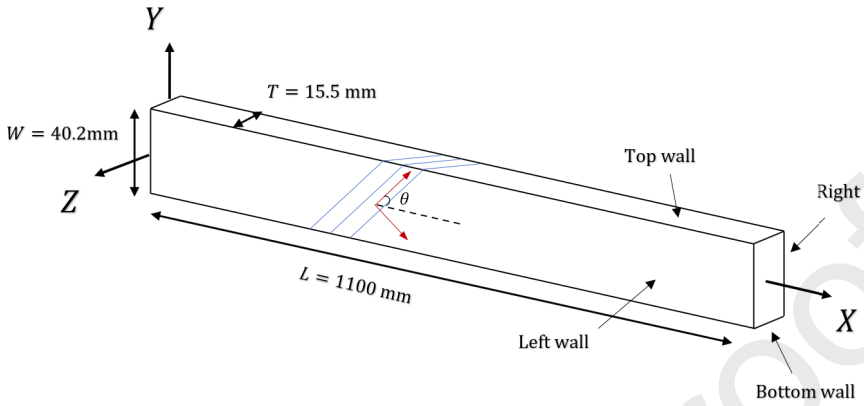

(a)

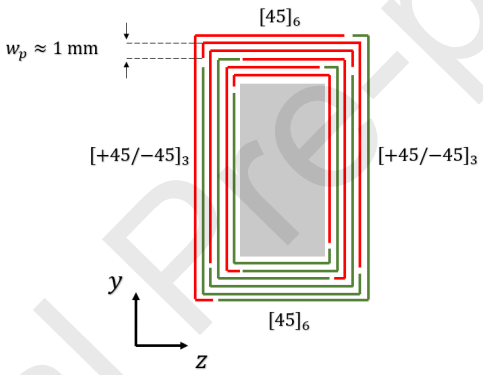

(b)

Figure 2: Schematic drawing of the specimen (a) geometry (b) layup configuration.

points were pre-selected, denoted L_2,L_1,C,R_1 and R_2, with a spacing of 50mm between each. The point C indicates the location of the shear centre where the application of loads will generate zero torque. In contrast, a combined torque and moment will be applied to the beam for the masses placed at the other loading points.

The strain distribution on the beam was measured using rectangular strain rosettes as shown in Figure 4. Each rosette includes three measuring grids arranged at angles of 0° and +45°/-45° to allow for the measurement of both axial and shear strain at the target point. The axial strain was directly measured

Figure 3: The vacuum bagged beam inside the autoclave.

from the 0° grid, while the shear strain,γ, was calculated based on the values acquired from the +45° and -45° grids:

$$\gamma = \frac{\varepsilon_{45^\circ} - \varepsilon_{-45^\circ}}{2} \tag{1}$$

Four strain rosettes were installed on the top wall (SG1 to SG4) along the centre line to characterise the strain distribution in the spanwise direction as shown in the Figure 4. Three additional strain rosettes (SG5, SG6 and SG7) were bonded to the left and bottom walls to measure the strain distributions across the beam section. The locations of the strain gauges were chosen according to a preliminary finite element analysis (FEA) to avoid the effects caused by the root fixture.

The deflection and twist of the beam were captured using a set of Omron laser sensors ZX2-LD 100, which offer a measurement range of 100 ± 35mm and resolution of 5μm, sufficient to provide accurate measurements. Two types of sensor configurations were adopted, as shown in Figure 6. For the deflection measurement, a single laser sensor was mounted approximately 100mm above the top wall of the beam. To measure the twist angle, a rigid foam strip was firstly aligned and clamped to the beam and then the angle of twist, ϕ, was evaluated by measuring the transverse displacements of the foam strip using two sensors installed vertically:

$$\phi = \tan^{-1}(\frac{\Delta d}{d_0}) \tag{2}$$

where the Δd indicates the difference in the transverse displacements measured from two locations and d_0 is the vertical distance between the sensors. For each loading condition, the measurements were repeated at 9 different locations along the beam span to evaluate the distribution of the deflection and twist.

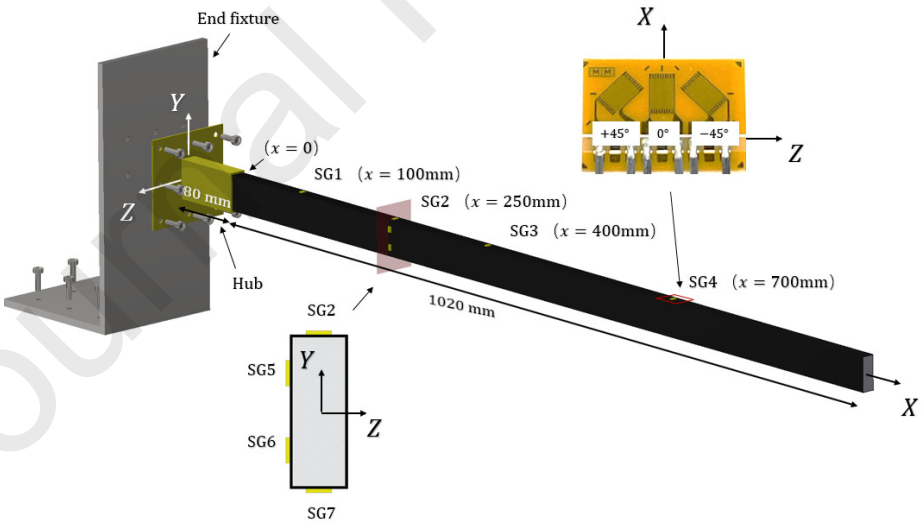

Figure 4: Strain gauge configuration on the beam.

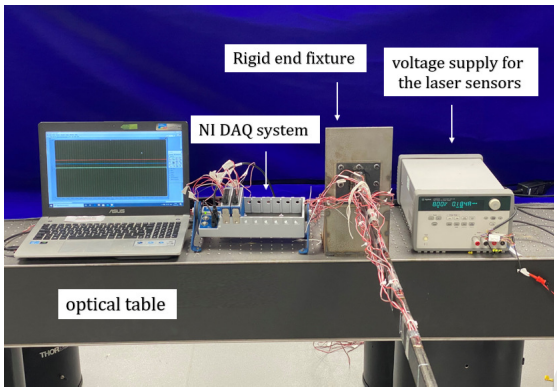

(a)

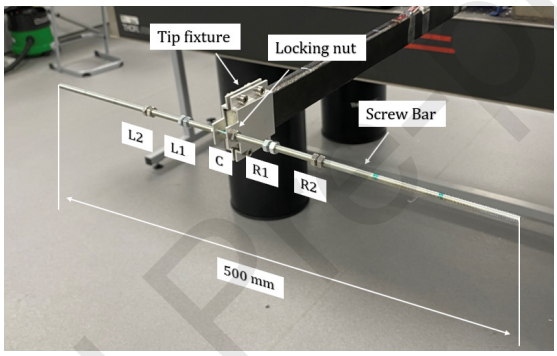

(b)

Figure 5: Experiment configurations: (a) assembly at the supporting end (b) fixture at the tip.

2.3. Numerical prediction

Finite element analysis (FEA) of the bend-twist coupled beam was performed using the commercial package ABAQUS 2017 [27]. The motion at the supporting end was fixed in all directions to replicate the condition of the experiment. The laminate behaviour was modelled using 4-noded three-dimensional shell elements with reduced integration (element code S4R in ABAQUS). Approximately 40 thousand elements were used in the model, which was sufficient for the simulation according to a preliminary mesh refinement study. The influence of the foam core was simulated by adding a layer of elastic isotropic

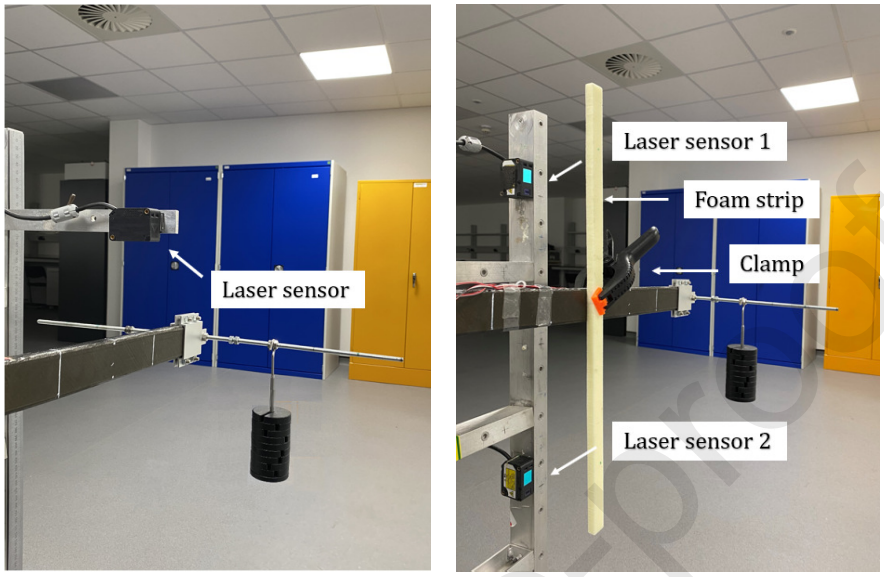

(a) (b)

Figure 6: Omron sensor configurations for the measurement of (a) deflection and (b) twist.

laminate into the thin-walled beam model created with Young's modulus and Poisson's ratio of 180 MPa and 0.42 respectively [26]. The effect of the staggered joints was neglected in the model where the laminate on each wall was assumed to be jointed perfectly at each edge with no prolonged plies. The tip fixture was simulated by mounting a 500mm long rigid shell to the tip of the beam model using the tie constraint as shown in Figure 7. The laminate properties used in the model are listed in Table 2. The deflection distribution of the beam model was obtained by plotting the vertical displacement of the beam along the centre line of the top surface, while the angle of twist was calculated from the transverse displacements of the top and bottom edges of the side wall using Eq. 2.

E_{11} (GPa)	E_{22}(GPa)	G_{12} (GPa)	v_{12}	ρ (kg/m^3)
154	8.9	5.3	0.32	1400

Table 2: Material properties used in the finite element(FE) model.

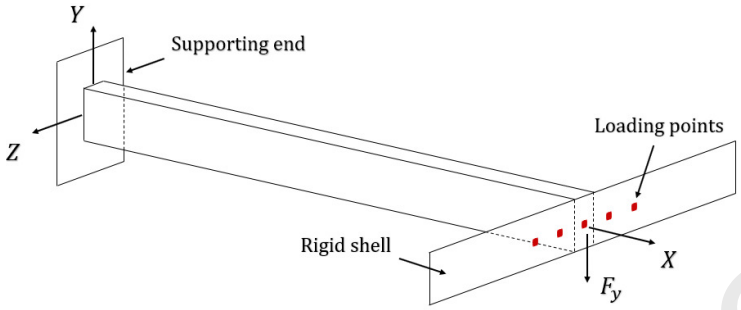

Figure 7: FE model configuration.

3. Results

3.1. Deflection and twist

Figure 8 presents the deflection of the beam when a mass of 1200g was placed at the tip, where the marker points represent the measured results and the solid curves are the numerical predictions obtained from FEA. Small differences in deflection have been found when the weight was applied at different loading points: more deflection is obtained by adding the mass at L2, compared to that at C and R2. This effect is caused by the influence of the applied torque which induces an additional bending moment to the beam, leading to the change in curvature.

The bend-induced twist has been measured and is shown in Figure 9. It was found that the FE predictions correspond very well with the experimental results, with only a small discrepancy likely caused by some occasional manufacturing defects occurring in vicinity of the ply drops at corners as shown in Figure 2(b) such as wrinkles. Note that the twist distribution significantly depends upon the location of the mass as a result of the applied torque. An increased twist was observed, when the mass was placed at the loading points L1 and L2, suggesting the applied torque twisted the beam in the same direction to the bend-induced torque. While for the mass placed at R1 and R2, lower angles of twist were measured, because the bend-induced torque was partially balanced by the torque produced by the weight. It was also noted that when

the mass was placed at R2, the maximum angle of twist occurred at 60% of the span, $X/L = 0.6$, indicating the magnitude of the applied torque was equal to the bend-induced torque arising at the beam section.

3.2. Strain distribution

Figures 10 and 11 show the spanwise distribution of the axial and shear strain for the masses placed at the shear centre (location C). The square markers denote measured results obtained from the strain gauges SG1 to SG4 as illustrated in Figure 4, while the solid lines represent the FEA predictions. It was found that both axial and shear strain changes linearly along the beam span, despite the noticeable end effect in vicinity to the supporting end. Scatter was also observed in the measured data, particularly for the measured shear strain, which was most likely caused by the differences in the bonding condition of the stain gauge due to the inconsistent surface finish on the beam surface.

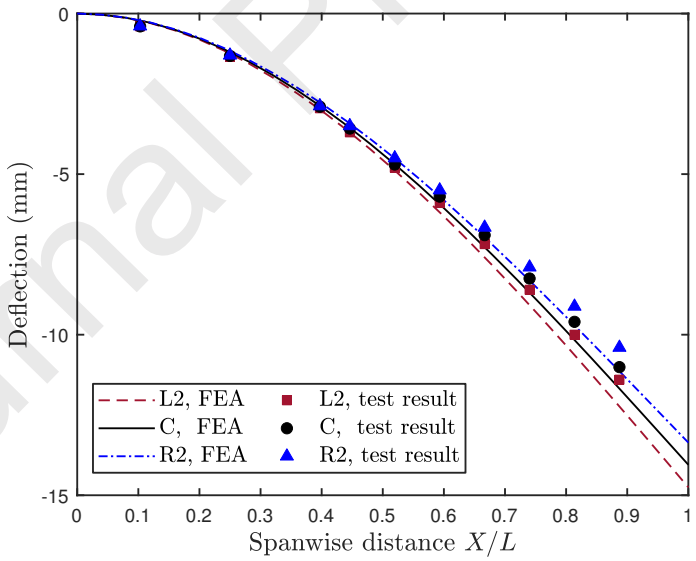

Figure 8: Distribution of the beam deflection with respect to a 1200g mass placed at different loading points.

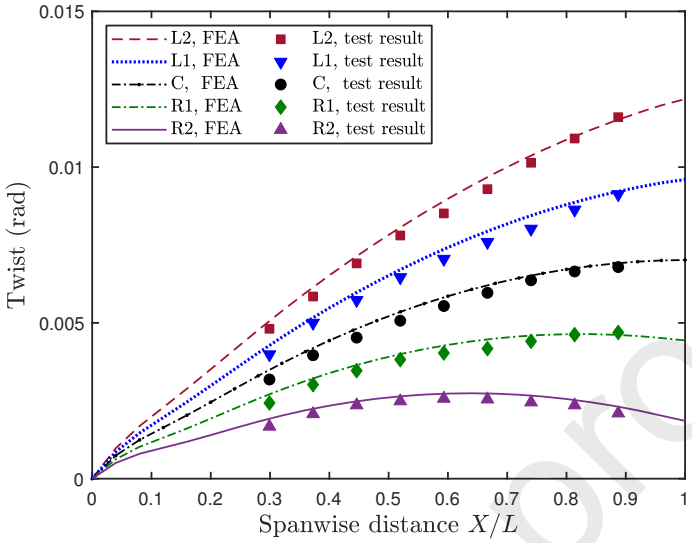

Figure 9: Distribution of the twist with respect to a 1200g mass placed at different loading points.

The strain distribution across the beam section was measured from strain gauges SG2, SG5, SG6, SG7, and the results are presented in Figures 12 and 13. The axial strain varies linearly with the beam thickness which satisfies the kinematic assumptions of beam theories. Both experimental data and numerical results suggest that the shear strain on the top and bottom walls are significantly higher than that in the side walls as shown in Figure 14. This is due to the extension-shear coupling behaviour exhibited in the $[45]_6$ laminate: a significant shear strain was induced by the axial strain produced by the bending moment, M_z. Besides, the laminate analysis suggested that the shear rigidity of the $[\pm 45]_3$ laminates were equal to 39.5 GPa, approximately 5 times that of the $[45]_6$ laminate, and this is another likely cause for the high shear strain in the top and bottom walls.

A minor difference in the axial strain was observed when the mass was placed at different loading points as shown in Figure 15 and 16. A slightly higher axial strain was observed when the mass was placed at L2 compared to that measured from other loading points, which agrees well with the measured

deflection curves shown in the Figure 8. The switch of the loading points resulted in a significant change in the shear strain shown in Figures 17, 18 and 19. It was found that the shear strain increased when the mass is moved toward to L1 and L2, indicating a higher torque was applied to the beam. Conversely, when the mass was applied to the other side of the shear centre i.e. R1 and R2, the overall torque was reduced which also verified the phenomenon observed in Figure 9. Furthermore, it is also shown in Figure 17 that the bending induced shear strain is significantly higher than that caused by the applied torque near to the root.

3.3. Simplified beam analysis

Based on the work of Hodge [28], the bend-twist behaviour of an anisotropic composite beam can be described by the following linear equations in matrix form:

$$\begin{bmatrix} T_x \\ M_z \end{bmatrix} = \begin{bmatrix} \overline{GJ} & -g \\ -g & \overline{EI} \end{bmatrix} \begin{bmatrix} \phi_x^{'} \\ k_z \end{bmatrix} \tag{3}$$

The above 2 by 2 matrix is known as the stiffness matrix of the beam, with g being the coupling term, and $\overline{GJ}$ and $\overline{EI}$ are the effective torsional and bending rigidity. The variables T_x and M_z are the applied torque and bending moment, while k_z and $\phi_x^{'}$ are the corresponding curvature and rate of twist. The obtained FE results have been used to determine the quantities in the stiffness matrix. Note that the rate of twist, $\phi_x^{'}$, was equal to zero at 60% of the span in the case when a 1200g mass was applied at R2 shown in Figure 9. At the beam section where $\phi_x^{'} = 0$, Eq. 3 can be simplified as:

$$T_x|_{X/L=0.6} = -g\ k_z|_{X/L=0.6} \tag{4}$$

$$M_z|_{X/L=0.6} = \overline{EI}\ k_z|_{X/L=0.6} \tag{5}$$

Hence the values of g and $\overline{EI}$ can be obtained directly from these expressions where the curvature k_z was calculated based on the deflection curve given in Figure 8. The torsional rigidity, $\overline{GJ}$, can be evaluated by using the measured twist and deflection for the weight placed at the shear centre where the applied torque, T_x, was equal to zero. Therefore the $\overline{GJ}$ can be related to the bending curvature and rate of twist as:

$$\overline{GJ} = \frac{gk_z}{\phi_x'} \tag{6}$$

The calculated quantities of the stiffness matrix are listed in Table 3, and the values are compared to the results generated by the variational-asymptotic beam cross-sectional(VABS) analysis, a commercial code developed by Hodges and his co-workers [29]. Compared to the three-dimensional FE model described in Sec. 2.3, VABS simplifies the three-dimensional problem into a two-dimensional cross sectional analysis and one-dimensional beam analysis with the aid of the variational asymptotic method [30, 31]. The quantities of the stiffness matrix are determined based on the evaluated three-dimensional warping function and the corresponding strain energy within the beam cross section. It is shown that the torsional rigidity calculated from the experimental results matches well with the FEA prediction. However, the measured bending rigidity and the coupling term is about 20% higher than the FEA predicted values, which is mainly due to the discrepancy between the measured deflection and the FE results, as shown in Figure 8. Furthermore the bending rigidity evaluated from the three-dimensional finite element model agrees well with the VABS results but the torsional rigidity $\overline{GJ}$ and the coupling term, g, calculated by VABS are approximately 15% higher than the FEA predictions. This discrepancy is attributed to two factors: (i) the neglect of a second order effect, a small flapwise bending curvature, k_y, (approximately 1% of the k_z) induced by the applied torque, T_x, was ignored in the current formulation for the sake of the simplicity, which resulted in a small underestimation of the torsional rigidity; (ii) the presence of

the end effect in the three-dimensional FE model: the shear stress concentration occurs near to the supporting end and leads to a significant effect in the local twist distribution which has not been considered in the simplified beam model adopted in VABS. It can be observed from Figure 9 that the influence of the
265 end effect is significant for $X/L < 0.1$.

	Bending rigidity, $\overline{EI}$ (N m^2)	Torsional rigidity, $\overline{GJ}$ (N m^2)	Coupling term, g (N m^2)
Experiment	390	210	96
FEA	310	220	75
VABS	320	260	89

Table 3: Comparison of the quantities in the stiffness matrix evaluated from experimental data, FEA and VABS.

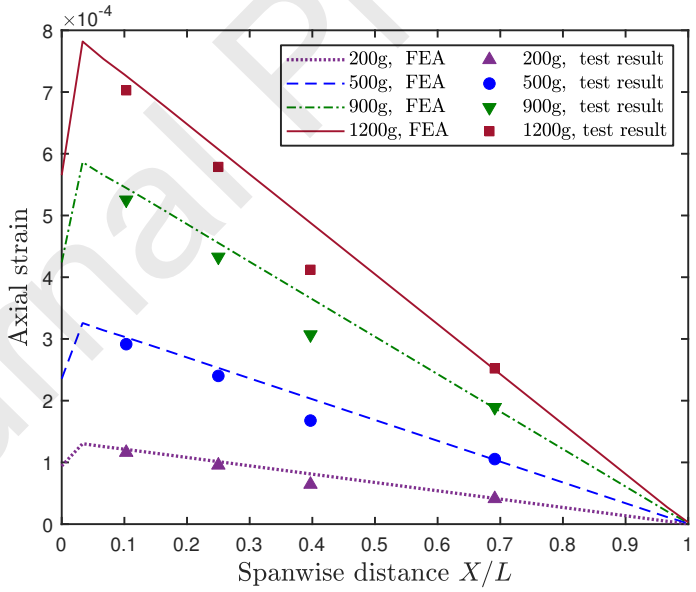

Figure 10: Distribution of the axial strain along the spanwise direction.

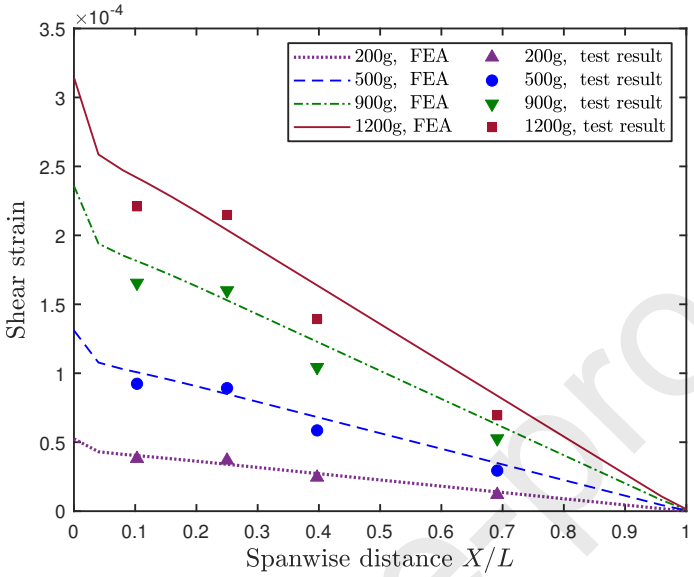

Figure 11: Distribution of the shear strain along the spanwise direction.

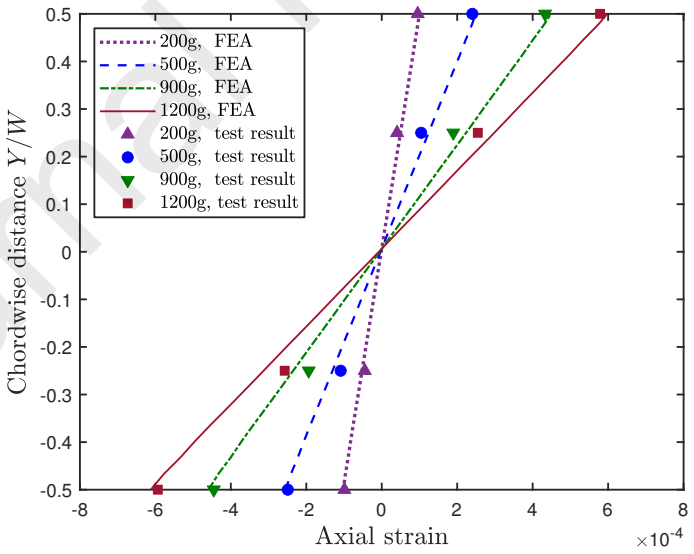

Figure 12: Distribution of the axial strain across the section.

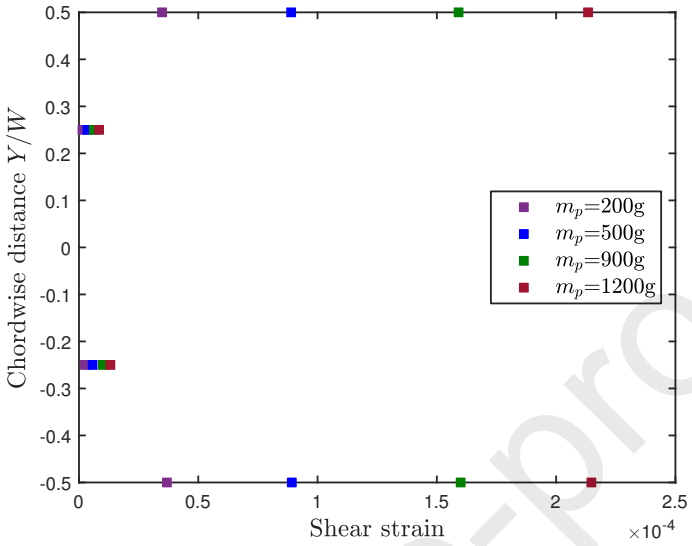

Figure 13: Distribution of the measured shear strain across the section.

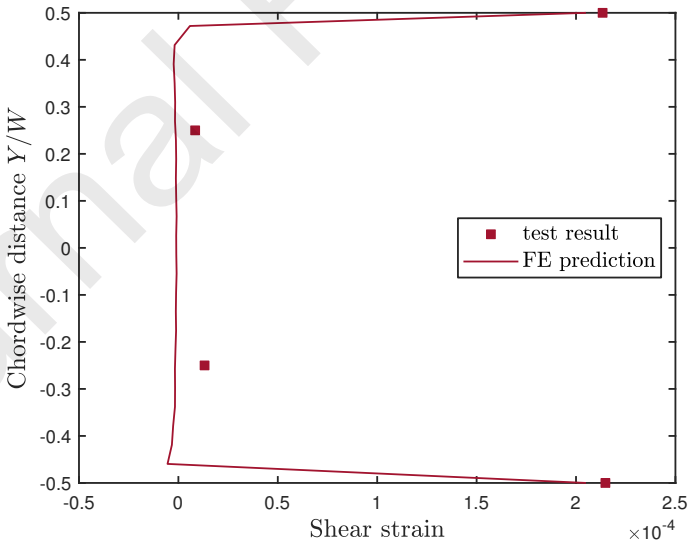

Figure 14: Comparison between the measured shear strain across the section with FE predictions subjected to a mass, m_p, of 1200g.

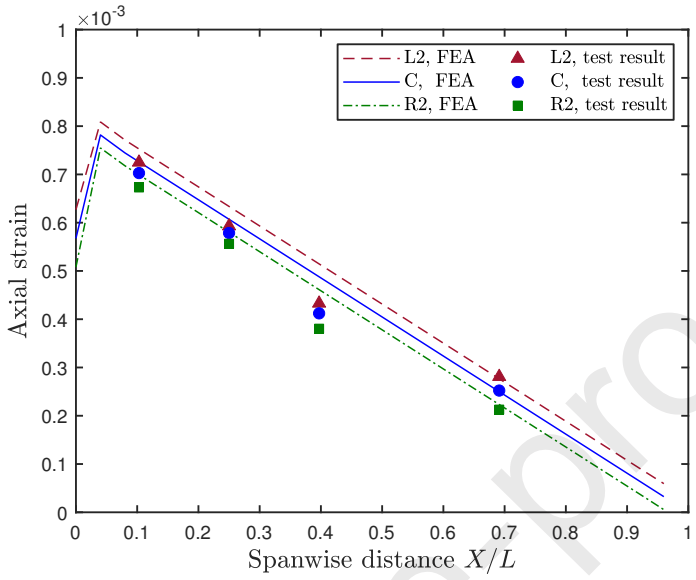

Figure 15: Spanwise axial strain distribution with respect to the mass added on different loading points.

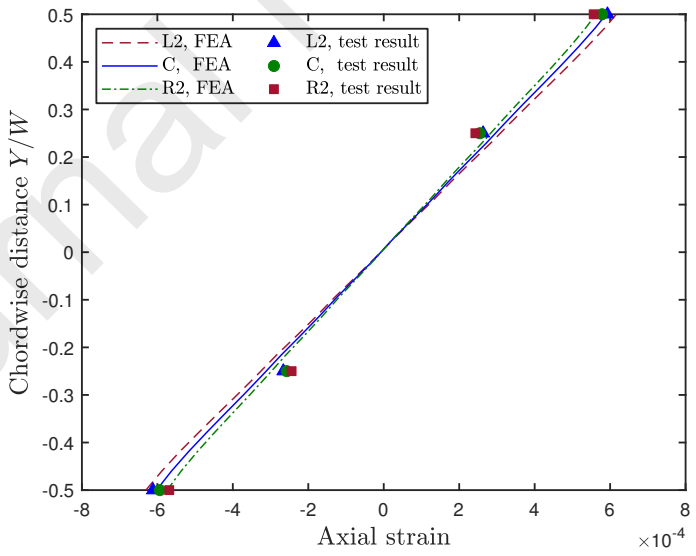

Figure 16: Axial strain distribution across the beam section with respect to the mass added on different loading points.

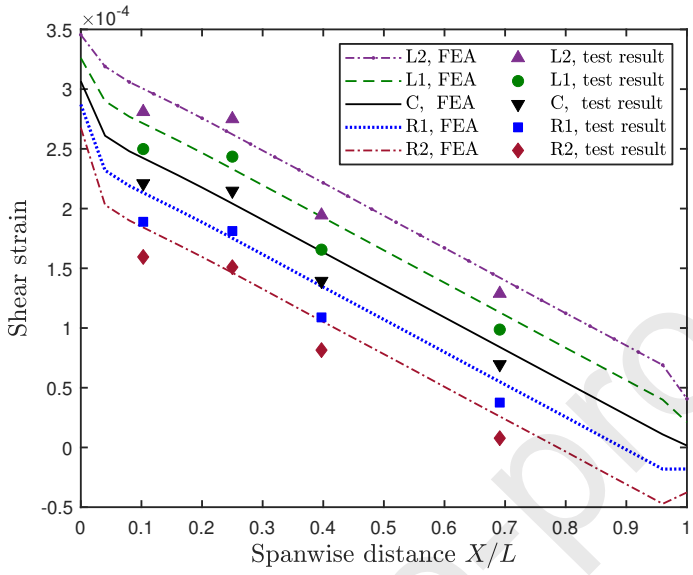

Figure 17: Spanwise shear strain distribution with respect to the mass added on different loading points.

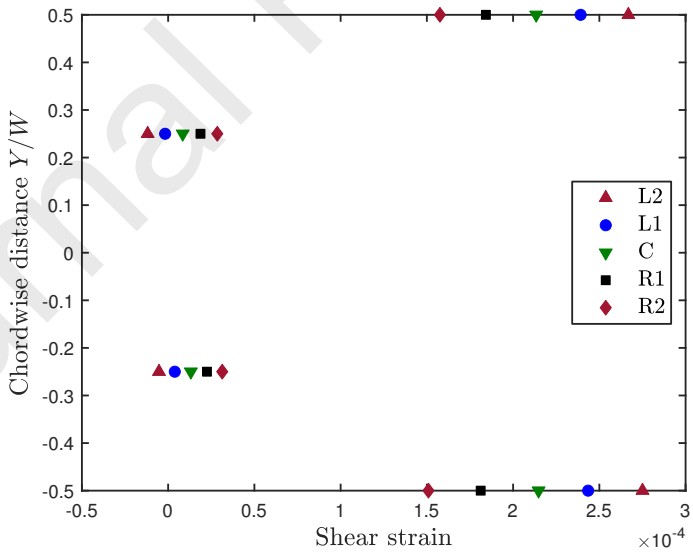

Figure 18: Shear strain distribution across the beam section with respect to the mass added on different loading points.

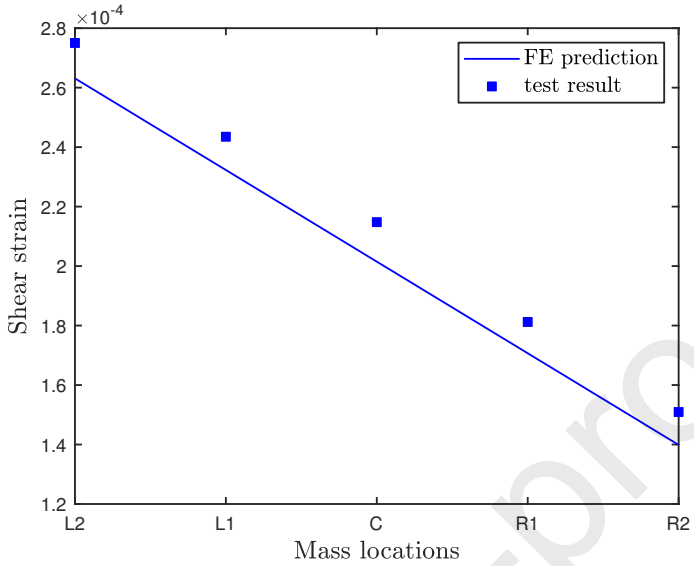

Figure 19: Comparison between the measured shear strain on the top surface (SG2) and FE prediction for the mass placed at different loading points.

4. Inertial twist concept

In this section, a passive twist morphing concept is examined using FEA, where a schematic drawing of the model configuration has been illustrated in Figure 20. The beam dimensions and material properties were identical to the experimentally verified model described in section 2.3. The rigid shell was mounted to the tip of the beam model using the tie constraint in ABAQUS which allowed for the inertial mass to be applied at different chordwise locations, y_p. The tip mass, m_p, was simulated by assigning the inertial property to the element at the target locations on the rigid shell. A rotational body force was then applied on the whole model to replicate the loading condition of a rotor blade.

Figure 21 presents the twist distribution of the beam subjected to a rotational speed of 1000 rpm, corresponding to a 20g inertial mass applied at the chordwise location $y_p = 25$ mm. It was found that the twist changes quadrati-

cally along the span, due to the distribution of the bending moment, M_z:

$$M_z = F_c \cos\beta y_p - F_c \sin\beta (L - X) \tag{7}$$

The two terms in Eq. 7 are the bending moment, M_z, produced from the two components of the centrifugual force, F_c, that are in parallel and perpendicular to the beam span, and the β is the angle between the F_c and the spanwise direction. Consequently, the overall bending moment increases with the spanwise distance, X. However, for the main rotor blade of a helicopter, the length of the blade span is usually tens of the chord length which will result in a small angle, β, and leads to a relatively constant bending moment distribution in the blade. Figure 22 presents the tip twist of the beam with respect to a number of inertial masses applied at different chordwise locations, y_p. The results show that the tip twist changes linearly with the chordwise locations, y_p, suggesting the desired twist can be obtained by a careful manipulation of the size and position of the inertial mass during the flight.

The analysis has been repeated for the beam models created with different ply angles ranged from 0° to 45° to investigate the optimum layup configuration. The results are presented in Figure 23 where the tip twist of each beam model is evaluated under the condition when a 20g mass placed at $y_p = 20$mm. It was found that the tip twist increased with the ply angle and the maximum twist was achieved at 40°, suggesting this ply angle will provide the highest actuation efficiency. To verify this conclusion, Eq. 3 has been rearranged by calculating the inverse of the stiffness matrix:

$$\begin{bmatrix} \phi_x^{'} \\ k_z \end{bmatrix} = \frac{1}{\overline{GJ}\ \overline{EI} - g^2} \begin{bmatrix} \overline{EI} & -g \\ -g & \overline{GJ} \end{bmatrix} \begin{bmatrix} T_x \\ M_z \end{bmatrix} \tag{8}$$

The efficiency of the actuation is dictated by the magnitude of the twist that can be achieved for a given bending moment, M_z, because this means a smaller actuation energy will be required for the desired twist. According to Eq. 8, the rate of twist, $\phi_x^{'}$, subjected to a bending moment, M_z, can be expressed as:

$$\phi_x^{'} = \alpha M_z \tag{9}$$

where

$$\alpha = \frac{g}{\overline{GJ}\ \overline{EI} - g^2} \tag{10}$$

The above shows that the rate of twist, $\phi_x^{'}$, is proportional to the bending moment, M_z and the normalised coupling term, α. The greater the value of α, more twist will be achieve for a given bending load. The cross sectional analysis has been conducted to evaluate the α for different ply angles as shown in Figure 24, where the same conclusion can be drawn. Although the highest efficiency is obtained from a 40° ply angle, a 45° ply angle which provides a similar angle of twist at a given bending moment is recommended to use in practice due to the ease of manufacturing.

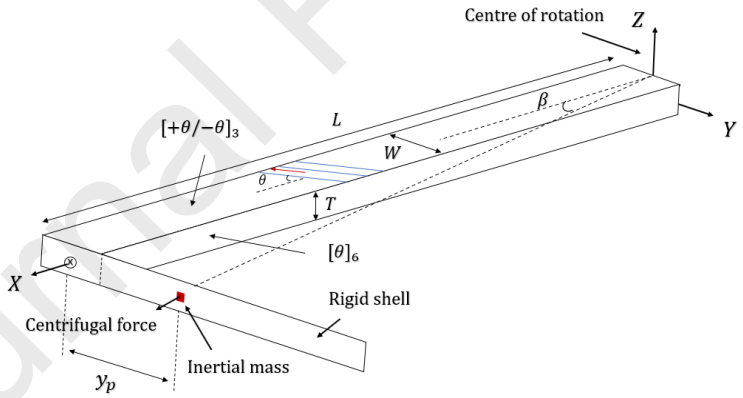

Figure 20: Schematic drawing the FE model for the demonstration of the inertial twist concept.

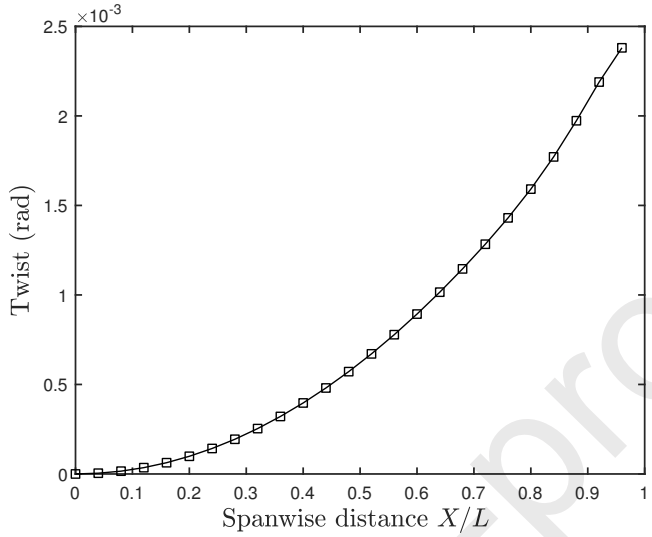

Figure 21: Twist distribution of the beam subjected to a rotational speed of 1000rpm (m_p=20g y_p = 25mm).

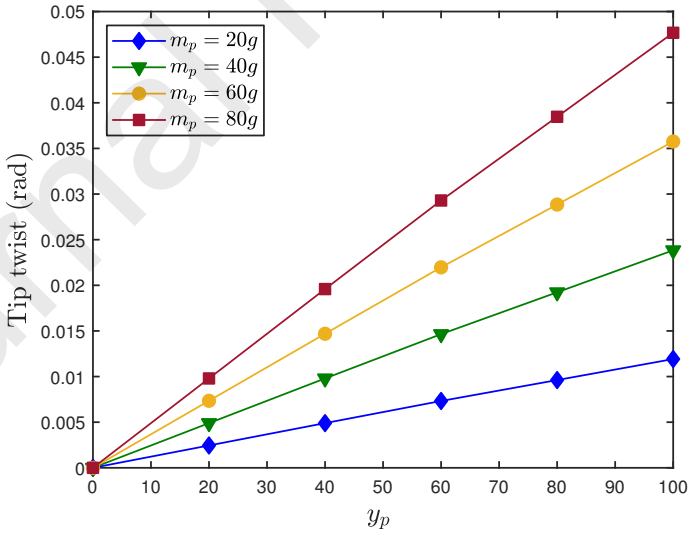

Figure 22: Tip twist of the beam with respect to different inertial masses,m_p, and chordwise locations, y_p under rotational speed of 1000rpm.

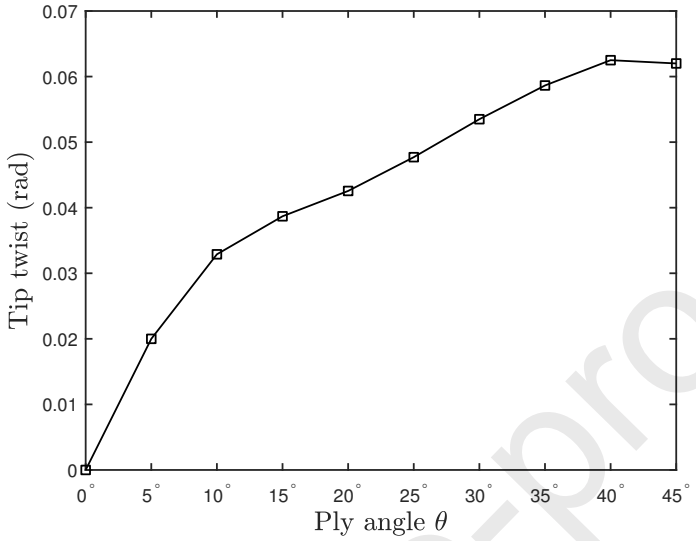

Figure 23: Comparison of the tip twist obtained from the beam models created with different ply angles (m_p=20g y_p = 25mm ω=1000rpm).

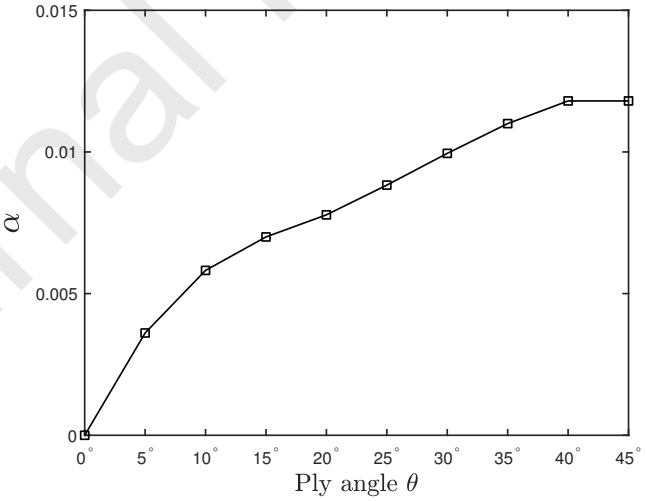

Figure 24: The normalised coupling term, α, of the beam models created by different ply angles.

5. Concluding remarks

In this paper, the application of the inertial twist concept has been examined for rotor blades. The numerical simulation has demonstrated the possibility that a reasonable amount of twist can be achieved by installing a relatively small mass at the blade tip. The numerical results also suggest that a 40° ply angle provides the highest actuation efficiency, where the greater twist angle can be obtained at a given bending moment compared to that of other ply angles. However, a 45° ply angle is considered to be implemented in practice due to the ease of manufacturing.

A set of bending tests has been performed using the composite beam manufactured with symmetric layup configuration. The detailed strain distribution and bend-twist property achieved in the beam were measured. The experimental data verified both FE predictions and the results produced from the simplified beam analysis (VABS), although the issues of the end effects e.g. the local stress concentration, caused some discrepancies between the results of FEA and VABS. The good agreement between the numerical and experimental results also verified the fabrication technique used for the beam manufacturing. It remains to determine the optimum aero-servo-elastic design of the morphing concept which allows for the maximum benefit to be attained at the overall system level.

Acknowledgement

The authors acknowledge funding from the European Union's Horizon 2020 project 'Shape Adaptive Blades for Rotorcraft Efficiency (SABRE)', under grant agreement 723491.

Reference

References

[1] S. Barbarino, O. Bilgen, R. M. Ajaj, M. I. Friswell, D. J. Inman, A review of morphing aircraft, Journal of Intelligent Material Systems and Structures 22 (9) (2011) 823–877.

[2] J. Fincham, M. Friswell, Aerodynamic optimisation of a camber morphing aerofoil, Aerospace Science and Technology 27 (2015) 245 – 255.

[3] D. Li, S. Zhao, A. D. Ronch, J. Xiang, J. Drofelnik, Y. Li, L. Zhang, Y. Wu, M. Kintscher, H. P. Monner, A. Rudenko, S. Guo, W. Yin, J. Kirn, S. Storm, R. D. Breuker, A review of modelling and analysis of morphing wings, Progress in Aerospace Sciences 100 (2018) 46 – 62.

[4] M. R. Motley, R. B. Barber, Passive control of marine hydrokinetic turbine blades, Composite Structures 110 (2014) 245 – 255.

[5] M. R. Amoozgar, A. D. Shaw, J. Zhang, M. I. Friswell, Composite blade twist modification by using a moving mass and stiffness tailoring, AIAA Journal 57 (2019) 4218–4225.

[6] M. Amoozgar, A. Shaw, J. Zhang, M. Friswell, The effect of a movable mass on the aeroelastic stability of composite hingeless rotor blades in hover, Journal of Fluids and Structures 87 (2019) 124–136.

[7] J. Sun, Q. Guan, Y. Liu, J. Leng, Morphing aircraft based on smart materials and structures: A state-of-the-art review, Journal of Intelligent Material Systems and Structures 27 (2016) 2289–2312.

[8] A. Ermakova, I. Dayyani, Shape morphing of aircraft wing: Status and challenges, Materials and Design 31 (2010) 1284 – 1292.

[9] E. Abdullah, C. Bil, S. Watkins, Application of smart materials for adaptive airfoil shape control, in: 47th AIAA Aerospace Sciences Meeting including The New Horizons Forum and Aerospace Exposition, 2009.

[10] S. M. Lim, S. Lee, H. C. Park, K. J. Yoon, N. S. Goo, Design and demonstration of a biomimetic wing section using a lightweight piezo-composite actuator (LIPCA), Journal of the American Helicopter Society 14 (2005) 496–503.

[11] P. C. Chen, I. Chopra, Induced strain actuation of composite beams and rotor blades with embedded piezoceramic elements, Smart Materials and Structures 5 (1996) 35–48.

[12] S. Ameduri, A. Concilio, A shape memory alloy torsion actuator for static blade twist, Journal of Intelligent Material Systems and Structures 30 (2019) 2605–2626.

[13] A. Bhattacharyya, D. C. Lagoudas, Y. Wang, V. K. Kinra, On the role of thermoelectric heat transfer in the design of SMA actuators: theoretical modeling and experiment, Smart Materials and Structures 4 (1995) 252–263.

[14] H. Prahlad, I. Chopra, Design of a variable twist tilt-rotor blade using shape memory alloy sma actuators, in: Smart Structures and Materials 2001: Smart Structures and Integrated Systems, Vol. 4327, SPIE, 2001, pp. 46 – 59.

[15] W. Raither, M. Heymanns, A. Bergamini, P. Ermanni, Morphing wing structure with controllable twist based on adaptive bending–twist coupling, Smart Materials and Structures 22 (2013) 065017.

[16] D. W. Lobitz, P. Veers, Aeroelastic behavior of twist-coupled hawt blades, ASME Wind Energy Symposium 21 (1998) 17–24.

[17] P. Shakya, M. R. Sunny, D. K. Maiti, A parametric study of flutter behavior of a composite wind turbine blade with bend-twist coupling, Composite Structures 207 (2019) 764 – 775.

[18] M. R. Motley, R. B. Barber, Study on composite bend-twist coupled wind turbine blade for passive load mitigation, Composite Structures 213 (2019) 173 – 189.

[19] R. Chandra, A. D. Stemple, I. Chopra, Thin-walled composite beams under bending, torsional, and extensional loads, Journal of Aircraft 27 (1990) 619–626.

[20] Y. Gibbs, Nasa armstrong fact sheet: X-29 advanced technology demonstrator aircraft, National Aeronautics and Space Administration (2017).

[21] R. Zhong, M. Fu, X. Chen, B. Zheng, L. Hu, A novel three-dimensional mechanical metamaterial with compression-torsion properties, Composite Structures 226 (2019).

[22] W. Wu, L. Geng, Y. Niu, D. Qi, X. Cui, D. Fan, Compression twist deformation of novel tetrachiral architected cylindrical tube inspired by towel gourd tendrils, Extreme Mechanics Letters 20 (2018) 104 – 111.

[23] N. Nayakanti, S. Tawfic, A. J. Hart, Twist-coupled kirigami cells and mechanisms, Extreme Mechanics Letters 21 (2018) 17–24.

[24] H. Gu, A. D. Shaw, M. R. Amoozgar, J. Zhang, C. Wang, M. I. Friswell, Twist morphing of a composite rotor blade using a novel metamaterial, Composite structures 254 (2020) 112855.

[25] BO 105 CB/CBS Approved Rotorcraft Flight Manual, 1993.

[26] EVONIK Inc., Rohacell XT data sheet (Available at: https://www.rohacell.com/product/rohacell/en/products-services/rohacell-xt/).

[27] ABAQUS/CAE user's manual : version 2017, ABAQUS.Inc., 2017.

[28] D. H. Hodges, in: Nonlinear Composite Beam Theory, American Institute of Aeronautics and Astronautics, 2006.

[29] VABS user's manual , AnalySwift Inc., 2011, Available at: http://analyswift.com/wp-content/uploads/2012/10/VABS-Manual.pdf.

[30] C. E. S. Cesnik, D. H. Hodges, Vabs: A new concept for composite rotor blade cross-sectional modeling, Journal of the American Helicopter Society 42 (1997) 27–38.

[31] W. Yu, D. H. Hodges, Generalized timoshenko theory of the variational asymptotic beam sectional analysis, Journal of the American Helicopter Society 50 (2005) 46–55.